Contingency-Aware Spatiotemporal Optimization for Safe Autonomous Vehicle Trajectory Planning

Zhihao Lin[1], Jianglin Lan[1,§], Anh-Tu Nguyen[2], *Senior Member, IEEE*, and David Flynn[1]

***Abstract*—Autonomous lane changing requires balancing safety, comfort, and efficiency while managing complex spatiotemporal vehicle interactions. Current methods often separate risk assessment from trajectory planning, leading to either conservative or unsafe maneuvers. This paper presents a contingency-aware spatiotemporal optimization framework that integrates dynamic risk assessment and trajectory optimization to ensure the autonomous host vehicle (HV) achieve safer, more efficient lane changes. First, the HV uses a dynamic risk field method to assess the collision risk with surrounding vehicles (SVs) in real-time, integrating dynamic obstacle interactions through modified Gaussian distributions. Second, a spatiotemporal safety corridor construction scheme leverages regression-based boundaries to transform spatiotemporal requirements into manageable optimization constraints. Third, the HV adopts a contingency-aware model predictive control framework that incorporates SVs uncertainty for human-like lane changes. The formulated optimization problem is solved using sequential quadratic programming with stability and recursive feasibility. Simulations confirm that our approach ensures safety and comfort of the HV across lane changing scenarios, achieving smoother trajectories, improved stability, and enhanced safety margins, with up to 95% reductions in longitudinal and lateral accelerations and a 27% decrease in lane-changing time.**

***Index Terms*—Autonomous vehicle, dynamic risk field, lane changing, model predictive control, trajectory planning.**

I. INTRODUCTION

AUTONOMOUS vehicles (AVs) have demonstrated significant potential in enhancing transportation safety and efficiency by reducing human errors and improving decision-making accuracy [1]. Lane changing represents one of the most challenging autonomous driving tasks, due to its requirement for real-time decision making while considering complex interactions with multiple surrounding vehicles (SVs) [2], [3]. During such maneuvers, the autonomous host vehicle (HV) faces numerous challenges (see Fig. 1): following a lead SV too conservatively may result in missed opportunities, while aggressive lane changes could lead to collision with SVs in the target lane [4]. Lane changing is complex because it must blend smoothly with traffic while staying safe and efficient [5]. Traditional approaches treating lane changing and car-following as separate processes often leading to inconsistent or suboptimal behaviors [6], [7]. In lane changes, autonomous HVs must balance dynamic interactions and static constraints to choose collision-free paths [8], demanding a unified approach that addresses both immediate safety and long-term trajectory planning [9].

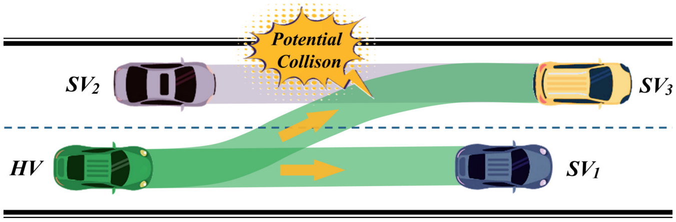

Fig. 1: During lane-changing, the autonomous host vehicle (HV) needs to interact with surrounding vehicles (SVs) to make accurate decisions and plan collision-free trajectories. The green transparent region represents potential trajectories of the HV, with the arrows indicating HV's movement directions.

Existing research on autonomous lane changing is broadly categorized into rule-based, learning-based, and optimization-based methods. Rule-based methods [10], [11] use predefined criteria for lane changes, offering efficiency but struggling in complex or unexpected traffic scenarios. Learning-based methods [12]–[14] handle diverse traffic by learning from data but face key challenges: 1) lack of formal safety guarantees, 2) limited interpretability, and 3) unpredictability in unseen scenarios [15], [16]. Optimization-based methods structure planning as constrained problems, but often use simplistic risk models that overlook dynamic traffic interactions.

Recent advancements have explored situation-based planning methods that integrate predictive capabilities with formal guarantees [17]. Rapidly-exploring Random Tree (RRT) and its variants generate space-filling trees for AV navigation [18], [19], aiding in obstacle avoidance. However, they face issues like slow convergence, high computational cost in complex spaces, and jerky, suboptimal trajectories [20]. Voronoi-based methods [21], [22] are efficient and safe in static settings, but struggle with dynamic obstacles and sparse sampling. The Artificial Potential Field (APF) method [23] offers intuitive obstacle avoidance, but often causes unstable trajectories and local minima traps [24]. Though better than traditional methods, these situation-based approaches focus on current states and lack foresight for evolving traffic [25], [26].

This work was supported in part by the China Scholarship Council Ph.D. Scholarship for 2023-2027 (No.202206170011), in part by the Leverhulme Trust Early Career Fellowship (ECF-2021-517), in part by the EPSRC Digital Twinning Research Hub for Decarbonising Transport (TransiT, Ref: EP/Z533221/1), and in part by the EPSRC Research Hub for Decarbonised Adaptable and Resilient Transport Infrastructures (DARe, Ref: EP/Y024257/1).

[1] Zhihao Lin, Jianglin Lan, and David Flynn are with the James Watt School of Engineering, University of Glasgow, Glasgow G12 8QQ, United Kingdom.

[2] Anh-Tu Nguyen is with the LAMIH UMR CNRS 8201 Laboratory, Université Polytechnique Hauts-de-France, 59313 Valenciennes, France, and also with INSA Hauts-de-France, 59313 Valenciennes, France.

[§] Corresponding author: Jianglin Lan (e-mail: jianglin.lan@glasgow.ac.uk)

Predictive optimization methods, like nonlinear model predictive control (NMPC), incorporate future state estimation for trajectory planning [27], [28]. However, NMPC faces challenges: 1) high computational cost, 2) sensitivity to prediction errors, and 3) difficulty modeling interactive behaviors [29]. Monte Carlo Tree Search (MCTS) methods balance exploration and exploitation to handle large state spaces [11], [12], but tightly coupling decision-making and planning hinders verification and error recovery. Space-time planning [10] is theoretically elegant but relies on simplified risk models and faces scalability issues in complex traffic.

A key gap in current literature is the separation of risk assessment and trajectory planning. Though some integrate risk metrics [30], they rely on simple models that miss complex spatial-temporal interactions in lane changing. Additionally, most treat SVs as reactive, not interactive agents [31], [32]. This leads to systems that are either overly conservative, missing opportunities, or too aggressive, risking safety in dynamic traffic.

To tackle these challenges, we propose an autonomous lane-changing framework integrating dynamic risk assessment, spatiotemporal safety corridors, and contingency-aware trajectory optimization. Simulations show our method outperforms existing ones by reducing acceleration variations and maintaining safety across scenarios. The main contributions and innovations of this work are:

1) We develop a dynamic risk field (DRF) method that combines static and dynamic risks using modified Gaussian distributions, reshaping risk distributions by motion direction for anticipatory assessment with a smooth, differentiable model capturing complex spatiotemporal interactions.
2) We introduce an innovative spatiotemporal safety corridor approach with regression-based boundary estimation that adaptively constructs phase-dependent safety regions, automatically activating relevant constraints based on the vehicle's position during lane transitions without requiring extensive training data or predetermined templates.
3) We propose a contingency-aware NMPC framework that incorporates the prediction uncertainty for SVs. The framework adapts trajectory optimization by selecting the best path based on anticipated responses of the target lane's rear SV, resulting in safer lane changes even under significant behavioral uncertainty.

The rest of this paper is organized as follows: Section II presents the problem formulation and system architecture. Section III details the dynamic risk awareness. Section IV describes spatiotemporal safety corridor construction. Section V describes the trajectory optimization framework. Section VI presents simulation results and comparative analysis, and Section VII concludes the paper.

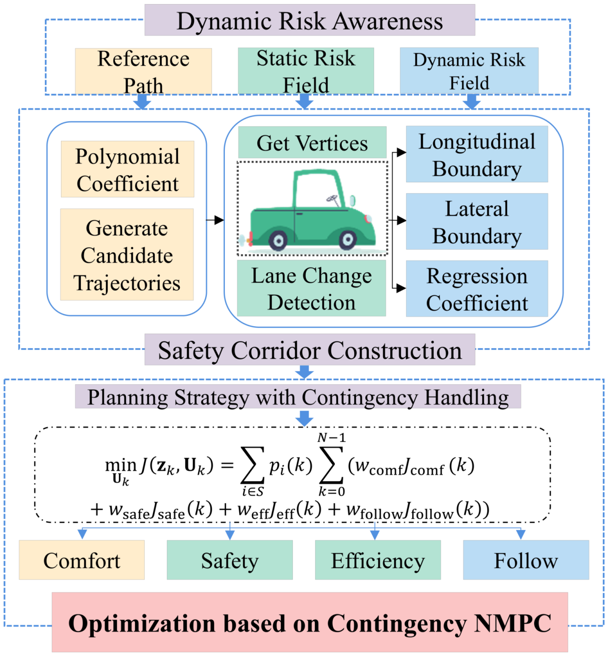

Fig. 2: The workflow of our proposed system.

II. PROBLEM DESCRIPTION AND SYSTEM STRUCTURE

This paper addresses the lane changing problem of planning safe, efficient trajectories for autonomous HVs amid dynamic environments with multiple SVs. Let $\mathbf{x}(t) = [s(t), v(t), a(t)]^\top$ be the HV's state vector at time t in the Frenet coordinate system, where $s(t)$ is the longitudinal position along the road centerline, $v(t)$ is the velocity, and $a(t)$ is the acceleration. The continuous-time vehicle dynamic model is represented by

$$\dot{s} = v, \ \ \dot{v} = a, \ \ \dot{a} = j \tag{1}$$

where j is the jerk. The constraints $v \in [v_{\min}, v_{\max}]$, $a \in [a_{\min}, a_{\max}]$ are imposed to ensure that the velocity, acceleration, and jerk remain within feasible bounds respecting vehicle dynamic capabilities and passenger comfort.

During lane changes, the autonomous HV needs to consider multiple SVs including the lead and rear vehicles in the current and target lanes, denoted as SV_1, SV_2, and SV_3 respectively (as shown in Fig. 1). For safety consideration, the minimum distance between HV and each SV_i should satisfy

$$|s(t) - s_i(t)| \geq d_{\text{safe}}(\kappa) \tag{2}$$

where $s_i(t)$ represents the longitudinal position of SV_i, and $d_{\text{safe}}(\kappa)$ is the adaptive safety distance that varies with the road curvature κ and relative velocities between HV and SV_i.

The lane changing problem is formulated as a prediction-aware optimization that considers multiple potential scenarios $i \in \mathcal{S}$, each with an associated probability $p_i(k)$. The optimization problem seeks the optimal control sequence (Fig. 2) minimizing a cost function with four key components:

$$\mathcal{J}(\cdot) = w_{\text{com}} J_{\text{com}} + w_{\text{saf}} J_{\text{saf}} + w_{\text{eff}} J_{\text{eff}} + w_{\text{fol}} J_{\text{fol}} \tag{3}$$

where J_{com} represents the comfort-related cost (jerk), J_{saf} evaluates collision risks under different predicted scenarios, J_{eff} promotes efficient lane changing execution, and J_{fol} ensures proper gap regulation in the target lane. The weights $w_{(\cdot)}$ balance these competing objectives.

To solve this constrained optimization problem, we propose a comprehensive hierarchical framework outlined in

Fig. 2, where the DRF block evaluates safety risks, the Safety Corridor module converts these risks into explicit constraints, and the NMPC optimizer generates trajectories that minimizes the cost function (3) whilst satisfying all the constraints. The detailed design of each component and their interactions will be presented in the following sections.

III. DYNAMIC RISK AWARENESS

This section presents the DRF method, integrating real-time risk evaluation with trajectory optimization to guide the HV through complex environments while ensuring safety and comfort. To facilitate efficient planning, a reference path Γ is established, providing a baseline for optimization and risk assessment. By transforming vehicle motion from Cartesian to Frenet coordinates relative to Γ, the problem is simplified, focusing on deviations in longitudinal and lateral directions. Key components are detailed below.

1) Reference Path Γ Definition: The reference path Γ, parameterized as $\mathbf{r}(s)$, is defined by a sequence of discrete points $(x_i, y_i), i \in [1, n]$, in the global Cartesian coordinate system, where n is the number of waypoints. To ensure smooth transitions and continuous derivatives, we fit these points with cubic polynomials in both x and y directions as follows:

$$x_r(s) = \sum_{i=0}^{3} a_i s^i, \;\; y_r(s) = \sum_{i=0}^{3} b_i s^i \tag{4}$$

where s is the arc length along the path, and s^i denotes the i-th power of s. The polynomial coefficients a_i and b_i, $i \in [0, 3]$, determine the shape of the reference path in the x and y directions, respectively. The resulting reference path $\mathbf{r}(s) = [x_r(s), y_r(s)]^\top$ is continuous and twice-differentiable. The path curvature $\kappa(s)$ at any point s is calculated by

$$\kappa(s) = \frac{\dot{x}_r(s)\ddot{y}_r(s) - \dot{y}_r(s)\ddot{x}_r(s)}{(\dot{x}_r(s)^2 + \dot{y}_r(s)^2)^{3/2}} \tag{5}$$

where $\dot{x}_r(s), \dot{y}_r(s)$ and $\ddot{x}_r(s), \ddot{y}_r(s)$ are the first and second derivatives of $(x_r(s), y_r(s))$ with respect to s, respectively.

The transformation from the Cartesian coordinates (x, y) to Frenet coordinates (s, d) is given by

$$\begin{bmatrix} x \\ y \end{bmatrix} = \begin{bmatrix} x_r(s) \\ y_r(s) \end{bmatrix} + d \begin{bmatrix} -\sin(\theta_r(s)) \\ \cos(\theta_r(s)) \end{bmatrix} \tag{6}$$

where d is the lateral offset from Γ and $\theta_r(s) = \arctan 2(\dot{y}_r(s), \dot{x}_r(s))$ is the path heading angle at s. $\arctan 2(y, x)$ is the two-argument arctangent function that computes the angle between the positive x-axis and the line from the origin to point (x, y), with a range of $(-\pi, \pi]$. The vehicle heading angle ψ at position (s, d) can then be computed as $\psi = \theta_r(s) - \arctan 2(\kappa(s)d, 1)$.

2) Candidate Trajectory Generation: To generate smooth candidate trajectories, we adopt a quintic polynomial interpolation method in the Frenet coordinate frame as shown in Fig. 3. Using a normalized path parameter $\tau \in [0, 1]$, both longitudinal position s and lateral offset d are parameterized as quintic polynomials that ensure continuous transitions up to the second-order derivatives, as follows:

$$s(\tau) = \sum_{i=0}^{5} c_i \tau^i, \;\; d(\tau) = \sum_{i=0}^{5} d_i \tau^i \tag{7}$$

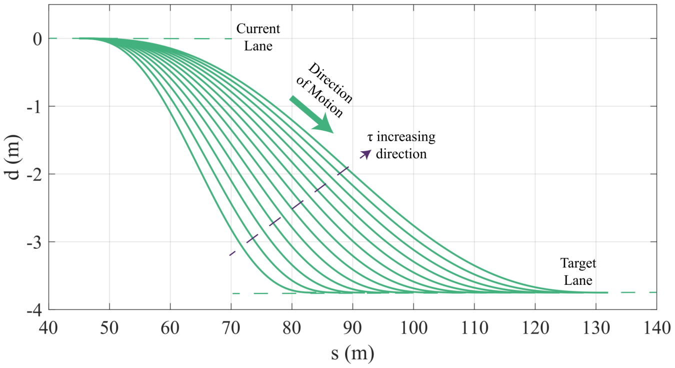

Fig. 3: Candidate trajectories generated using quintic polynomials in the Frenet coordinate system.

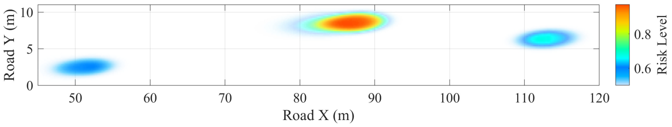

Fig. 4: Illustration of the dynamic risk field.

where τ^i denotes the i-th power of the normalized parameter τ. The coefficients c_i and d_i, $i \in [1, 5]$, are solved from

$$[\mathbf{T}_0 \;\mathbf{T}_1]^\top \mathbf{c} = [\mathbf{x}_s \;\mathbf{x}_e]^\top, \;\; [\mathbf{T}_0 \;\mathbf{T}_1]^\top \mathbf{d} = [\mathbf{y}_s \;\mathbf{y}_e]^\top$$

where $\mathbf{c} = [c_5 \; c_4 \; c_3 \; c_2 \; c_1 \; c_0]^\top$, $\mathbf{d} = [d_5 \; d_4 \; d_3 \; d_2 \; d_1 \; d_0]^\top$. $\mathbf{x}_s$, $\mathbf{x}_e$ and $\mathbf{y}_s$, $\mathbf{y}_e$ represent the longitudinal and lateral boundary conditions conditions at the start and end points, respectively. For the longitudinal motion, we have $\mathbf{x}_s = [s_s, v_s \cos(\theta_s), a_s \cos(\theta_s)]$ and $\mathbf{x}_e$=$[s_e, v_e \cos(\theta_e), a_e \cos(\theta_e)]$. For the lateral motion, the same logic applies with the corresponding lateral boundary conditions. The transformation matrices $\mathbf{T}_0$ and $\mathbf{T}_1$ encode the polynomial coefficients for evaluation and derivatives at $\tau = 0$ and $\tau = 1$ respectively:

$$\mathbf{T}_0 = \begin{bmatrix} 0 & 0 & 0 & 0 & 0 & 1 \\ 0 & 0 & 0 & 0 & 1 & 0 \\ 0 & 0 & 0 & 2 & 0 & 0 \end{bmatrix}, \mathbf{T}_1 = \begin{bmatrix} 1 & 1 & 1 & 1 & 1 & 1 \\ 5 & 4 & 3 & 2 & 1 & 0 \\ 20 & 12 & 6 & 2 & 0 & 0 \end{bmatrix}.$$

3) DRF Construction: The traditional APF typically model obstacles as static repulsive forces and they often struggle with dynamic environments due to their limited ability to model temporal interactions. Conversely, learning-based approaches can capture complex patterns but frequently lack interpretability and theoretical guarantees [33]. Our DRF method bridges this gap by extending Gaussian-based risk representations with explicit modeling of dynamic interactions through a velocity-dependent component.

Unlike existing methods that simply scale static risk fields based on relative velocity magnitude [34], our approach fundamentally reshapes the risk distribution based on both the magnitude and direction of relative motion. This allows the DRF to anticipate potential collisions by shifting risk concentration in the direction of relative motion while maintaining differentiability for optimization. The resulting risk field combines the mathematical tractability of traditional APF with enhanced spatial-temporal adaptivity that dynamically

TABLE I:
PARAMETER VALUES FOR THE DYNAMIC RISK FIELD.

Parameter	Description	Value
A_s	Static risk amplitude	1.0
A_d	Dynamic risk amplitude	0.7
σ_x	Longitudinal spatial std. dev.	$1.5l_v$
σ_y	Lateral spatial std. dev.	$1.2w_v$
β	Shape parameter	2.0
α	Position influence factor	2.0
k_v	Velocity scaling factor	0.4
d_e	Influence decay distance	8 m

l_v and w_v represent the vehicle's length and width, respectively.

responds to changing vehicle interactions without requiring complex modeling or extensive computational resources.

The DRF represents the potential collision risk between the HV and surrounding obstacles SVs. For each SV$_i$, we construct $R_i(x, y)$ that combines both position and velocity dependent risk components as follows:

$$R_i(x, y) = (R_{s,i}(x, y) + R_{d,i}(x, y))F_e(x, y). \tag{8}$$

The position-based risk field $R_{s,i}(x, y)$, as shown in Fig. 4, is modeled as a modified Gaussian distribution in the obstacle-centered coordinate system as follows:

$$R_{s,i}(x, y) = A_s \exp\Big(- \Big(\Big(\frac{\Delta x'}{\sigma_x}\Big)^2 + \Big(\frac{\Delta y'}{\sigma_y}\Big)^2\Big)^\beta\Big) \tag{9}$$

where A_s is the maximum amplitude of the static risk field, σ_x and σ_y are the spatial standard deviations that determine the spread of risk in longitudinal and lateral directions based on the vehicle dimensions, and β is a shape parameter controlling the rate of risk decay with distance. $(\Delta x', \Delta y')$ are the relative coordinates after rotation by the obstacle's heading angle θ_i:

$$\begin{bmatrix}\Delta x' \\ \Delta y'\end{bmatrix} = \begin{bmatrix}\cos(\theta_i) & \sin(\theta_i) \\ -\sin(\theta_i) & \cos(\theta_i)\end{bmatrix}\begin{bmatrix}x - x_i \\ y - y_i\end{bmatrix}.$$

The velocity-dependent risk $R_{d,i}(x, y)$ account for the relative velocity $v_{\text{rel}} = v_{SVs} - v_0$ between SVs and HV:

$$R_{d,i}(x, y) = \frac{A_d \exp\Big(-\frac{\Delta x'^2}{\sigma_v^2} - \frac{\Delta y'^2}{\sigma_y^2}\Big)}{1+\exp(-\text{sgn}(v_{\text{rel}})(\Delta x' - \alpha\sigma_x \text{sgn}(v_{\text{rel}})))} \tag{10}$$

where A_d represents the maximum amplitude of the DRF, $\sigma_v = k_v|v_{\text{rel}}|$ is the velocity-dependent spatial variance, and α is the position influence factor. This formulation introduces three key innovations: 1) σ_v automatically adapts safety margins based on v_{rel}; 2) A logistic denominator term creating an asymmetric risk distribution that shifts concentration based on relative motion direction—extending the field forward when SV$_i$ approaches HV ($v_{\text{rel}} < 0$) and behind SV$_i$ when HV approaches it ($v_{\text{rel}} > 0$); and 3) Decay factor $F_e(x, y)$ ensuring realistic risk diminishing with distance:

$$F_e(x, y) = \exp(-\sqrt{(x - x_0)^2 + (y - y_0)^2}/d_e). \tag{11}$$

Compared to learning-based methods [35], it provides greater interpretability and theoretical guarantees with lower computational cost, while avoiding the unstable trajectories often generated by APF approaches when handling dynamic obstacles.

Table I presents the parameter values used in our DRF formulation, which were determined through a combination of theoretical analysis and extensive experimental validation to ensure effective risk assessment across diverse traffic scenarios. The static risk amplitude A_s is set higher than the dynamic risk amplitude A_d to prioritize immediate collision risks over potential future conflicts. The shape parameter $\beta = 2$ creates a risk field that balances between a steep Gaussian ($\beta = 1$) and a broader platykurtic distribution, providing appropriate risk gradients for optimization. The spatial standard deviations σ_x and σ_y were selected based on typical highway lane widths (3.5–3.7 m) and vehicle dimensions, while σ_v scales with relative velocity to accurately represent the increased risk at higher closing speeds. The position influence factor α determines the asymmetry of the DRF, with $\alpha = 2$ creating a forward-shifted risk profile that anticipates motion. The influence decay distance d_e was set to ensure sufficient risk perception range while maintaining computational efficiency.

To validate the sensitivity of these parameters, we conducted a series of tests by varying each parameter within $\pm 30\%$ of its nominal value. The results indicated that the risk field maintains robustness across reasonable parameter variations, with performance degradation less than 5% in terms of safety margins and comfort metrics. The dynamic risk coefficient k_v and shape parameter β were found to be the most sensitive parameters, requiring careful tuning to balance safety conservatism with trajectory optimization efficiency.

IV. SPATIOTEMPORAL SAFETY CORRIDORS

This section outlines the construction of time-varying safety corridors based on spatial and dynamic relationships between the HV and SVs (Algorithm 1). These corridors define dynamic constraints used in the next section to ensure safe, collision-free lane changes.

Let v_i be the velocity of vehicle i, where $i \in [0, 3]$ with $i = 0$ representing the HV, and $i \in [1, 3]$ representing the SVs in the current lane front, target lane rear and front, respectively. The vehicle's geometric profile is defined by four vertices $\mathbf{V} = [\mathbf{v}_1, \mathbf{v}_2, \mathbf{v}_3, \mathbf{v}_4]$, obtained via rotation transformation:

$$\mathbf{v}_i = \mathbf{p} + \mathbf{R}(\theta)\mathbf{d}_i, \quad i \in [1, 4] \tag{12}$$

where $\mathbf{p} = [x, y]^\top$ is the vehicle's position in the Cartesian coordinate system, and θ is the heading angle. $\mathbf{R}(\theta)$ is the rotation matrix and $\mathbf{d}_i$ represents the displacement vectors incorporating vehicle dimensions, given by

$$\mathbf{R}(\theta) = \begin{bmatrix}\cos(\theta) & -\sin(\theta) \\ \sin(\theta) & \cos(\theta)\end{bmatrix}, \quad \mathbf{d}_i = \begin{bmatrix}\sigma_x l_\text{v}/2 \\ \sigma_y w_\text{v}/2\end{bmatrix} \tag{13}$$

where l_v and w_v are vehicle's length and width, and $(\sigma_x, \sigma_y) \in \{(1, 1), (1, -1), (-1, 1), (-1, -1)\}$ defines four vertices.

1) Safety Boundary Matrix Construction: The safety constraints vary by lane changing phases, determined by HV's lateral position relative to the lane centerline. Initially, boundaries are defined spatially and then converted to time-varying constraints for optimization. The lane changing includes three phases: 1) Pre-transition phase (ϕ_1), with constraints only from the initial lane front vehicle (SV$_1$); 2) Transition phase (ϕ_2), where all SVs constraints are active; and 3) Post-transition phase (ϕ_3), with constraints from target lane vehicles (SV$_2$,

Algorithm 1 Spatiotemporal safety corridor construction

```
Input: $\Gamma$, HV's state $\mathbf{x}_0$, and SVs' states $\{\mathbf{x}_i\}_{i=1}^{3}$
Discretize path with $L$ points: $\Delta s = s_g/L$
Initialize $\mathbf{S}_b \in \mathbb{R}^{L\times 6}$
for $l = 1$ to $L$ do
    Transform vehicle vertices to Frenet coordinates
    Calculate $s_{b1}(l), s_{b2}(l), s_{b3}(l)$ in (16)
    Determine $d_u(l), d_l(l)$ according to (17)
    Update $\mathbf{S}_b[l, :]$ with computed boundaries in (15)
end for
// Regression-based Boundary Estimation //
for each time step $k$ do
    Sample points: $\mathcal{L}_k$ in (19)
    Collect data points: $\mathbf{D}_k = \{(s_l, s_{bj}(l))\}_{l\in\mathcal{L}_k}$
    Compute regression coefficients $[\alpha_j(k), \beta_j(k)]$
    Construct regression vector $\mathbf{r}_{kj}$ in (22)
end for
Return: Safety boundary matrix $\mathbf{S}_b$
```

SV$_3$). Let $\mathbf{V}_{x,i}$ and $\mathbf{V}_{y,i}$ represent the sets of longitudinal and lateral coordinates of vehicle i's vertices. At time step k, we define $d_0^{\max}(k) = \max(\mathbf{V}_{y,0}(k)), d_0^{\min}(k) = \min(\mathbf{V}_{y,0}(k)), d_2^{\max}(k) = \max(\mathbf{V}_{y,2}(k))$, and $d_2^{\min}(k) = \min(\mathbf{V}_{y,2}(k))$. The phase function $\phi(k)$ at k is defined as

$$\phi(k) = \begin{cases} \phi_1, & d_0^{\min}(k) > d_{cl} \\ \phi_2, & d_0^{\min}(k) \le d_{cl} \text{ and } d_0^{\max}(k) \ge d_{cl} \\ \phi_3, & d_0^{\max}(k) < d_{cl} \end{cases} \tag{14}$$

where d_{cl} is the distance between the center lines of two lanes.

During the lane-change process, we discretize the path into L points with spacing $\Delta s = s_g/L$, with the path length s_g being estimated by $s_g = (s_f - s_s)\cdot \max(1, v_0/v_3)$, where s_f and s_s are the planned final and start positions, respectively. For each discretized point, we compute its Frenet coordinates and construct a safety boundary matrix $\mathbf{S}_b \in \mathbb{R}^{L\times 6}$ that includes both longitudinal boundaries ($s_{bi},\ i \in [1,3]$) and lateral boundaries (d_u, d_l):

$$\mathbf{S}_b = \begin{bmatrix} s_1 & s_{b1}(1) & s_{b2}(1) & s_{b3}(1) & d_u(1) & d_l(1) \\ \vdots & \vdots & \vdots & \vdots & \vdots & \vdots \\ s_l & s_{b1}(l) & s_{b2}(l) & s_{b3}(l) & d_u(l) & d_l(l) \\ \vdots & \vdots & \vdots & \vdots & \vdots & \vdots \\ s_L & s_{b1}(L) & s_{b2}(L) & s_{b3}(L) & d_u(L) & d_l(L) \end{bmatrix}. \tag{15}$$

The longitudinal boundaries $s_{bi},\ i \in [1,3]$, are determined by

$$\begin{aligned} s_{b1}(k) &= \begin{cases} \min(\mathbf{V}_{x,1}(k)) - d_{\text{safe}}(\kappa), & \text{if } \phi(k) \in \{\phi_1, \phi_2\} \\ \text{NaN}, & \text{if } \phi(k) = \phi_3 \end{cases} \\ s_{b2}(k) &= \begin{cases} \text{NaN}, & \text{if } \phi(k) = \phi_1 \\ \max(\mathbf{V}_{x,2}(k)) + d_{\text{safe}}(\kappa), & \text{if } \phi(k) \in \{\phi_2, \phi_3\} \end{cases} \\ s_{b3}(k) &= \begin{cases} \text{NaN}, & \text{if } \phi(k) = \phi_1 \\ \min(\mathbf{V}_{x,3}(k)) - d_{\text{safe}}(\kappa), & \text{if } \phi(k) \in \{\phi_2, \phi_3\} \end{cases} \end{aligned} \tag{16}$$

where NaN indicates inactive constraints, ensuring only relevant safety conditions are applied at each lane change stage. The lateral boundaries d_u, d_l are determined by

$$\begin{aligned} d_u(k) &= \begin{cases} \min(\mathbf{V}_{y,2}(k)) - d_{\text{safe}}(\kappa), & \text{if } \theta_2(k) \\ d_0^{\max}(k) + d_{\text{safe}}(\kappa), & \text{otherwise} \end{cases} \\ d_l(k) &= \begin{cases} \max(d_2^{\max}(k), d_0^{\min}(k)), & \text{if } \theta_2(k) \\ d_0^{\min}(k) - d_{\text{safe}}(\kappa), & \text{otherwise} \end{cases} \\ \theta_2(k) &\triangleq \max(\mathbf{V}_{x,2}(k)) \ge \min(\mathbf{V}_{x,0}(k)) \\ d_{\text{safe}}(\kappa) &= d_{\text{base}} + k_v|v_i - v_0| + k_\kappa|\kappa| \end{aligned} \tag{17}$$

where d_{base} is the minimum safety distance, k_v and k_κ are positive scaling factors, and $\theta_2(k)$ indicates longitudinal overlap with the SV$_2$. The lateral boundaries inherently handle the phase transitions through the vehicle geometry considerations.

2) Regression Coefficient Calculation: To convert spatial safety boundaries to time-varying continuous functions, we first define the time discretization as

$$t_k = k\Delta t, \quad \Delta t = T/I, \quad T = (s_f - s_s)/\min(v_0, v_3) \tag{18}$$

where I is the number of discretization steps, and T is the minimum time required for lane changing. Let $s_0(k)$ denote the longitudinal position of the HV at time step k. For each discretized path point indexed by $l \in [1, L]$, we denote its longitudinal coordinate as s_l. The set of relevant path point indices at k is described by

$$\mathcal{L}_k = \{l \mid l \in [1, L], s_l \in [s_0(k) - \Delta s, s_0(k) + \Delta s]\} \tag{19}$$

where Δs is the spatial sampling interval that defines the local regression window around the HV's current position.

For each time step k, we collect discrete data points $\mathbf{D}_k = \{(s_l, s_{bj}(l))\}_{l\in\mathcal{L}_k}$ and perform the following linear regression:

$$s_{bj}(k, s) = \alpha_j(k)s + \gamma_j(k),\ \forall s \in [s_s, s_f] \tag{20}$$

with regression coefficients $\alpha_j(k)$ and $\gamma_j(k)$ are calculated by

$$[\alpha_j(k)\ \beta_j(k)]^\top = \left(\mathbf{X}_k^\top \mathbf{X}_k\right)^{-1} \mathbf{X}_k^\top \mathbf{y}_{j,k} \tag{21}$$

where $\mathbf{X}_k = \begin{bmatrix} s(l_1) & 1 \\ \vdots & \vdots \\ s(l_m) & 1 \end{bmatrix}$, $\mathbf{y}_{j,k} = \begin{bmatrix} s_{bj}(l_1) \\ \vdots \\ s_{bj}(l_m) \end{bmatrix}$, $[l_1, l_m] \in \mathcal{L}_k$ with $m = |\mathcal{L}_k|$ as the number of points in the local regression window. For each longitudinal boundary j, we define

$$\mathbf{r}_{kj} = \begin{cases} [\alpha_j(k), \beta_j(k)], & |\mathcal{L}_k| \ge 2 \\ [\text{NaN}, \text{NaN}], & \text{otherwise} \end{cases}. \tag{22}$$

The lateral bounds $d_u(k)$ and $d_l(k)$ from (17) are used directly, as they remain constant for each time step k (see Algorithm 1). These bounds provide continuous constraints for trajectory optimization, as illustrated in Fig. 5.

We selected linear regression for boundary approximation due to its computational efficiency and closed-form solution, making it well-suited for real-time applications. This regression-based approach adapts to traffic scenarios through: 1) Dynamic construction of safety boundary matrix $\mathbf{S}_b$; 2) Continuous shifting of the regression window $\mathcal{L}_k$ around the vehicle's current position; and 3) Automatic constraint activation based on the phase function $\phi(k)$. Unlike methods that rely on offline learning or predefined templates [36],

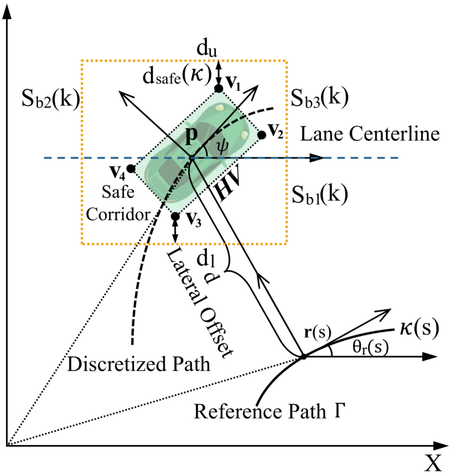

Fig. 5: Illustration of the spatiotemporal safety corridor.

our approach generates corridors in real-time, offering greater adaptability to unexpected scenarios with lower computational demands, while maintaining interpretability and theoretical guarantees that learning-based alternatives often lack.

V. TRAJECTORY OPTIMIZATION

This section formulates the lane changing trajectory planning as a constrained NMPC problem that incorporates prediction of the SV_2. Unlike traditional approaches that either assume fixed motion patterns or full cooperation for SVs, we recognize that vehicles (whether HDVs or AVs) naturally respond to merging maneuvers while maintaining their own preferences [37]. This observation motivates the proposal of a prediction-aware planning framework that adapts to SV_2's potential responses for safer and more efficient lane changes.

A. Planning Strategy with Contingency Handling

To implement this prediction-aware planning strategy, we first define the key components of our NMPC formulation. The problem is structured around the combined state space of both the HV and the target lane rear vehicle (SV_2), allowing us to explicitly consider their coupled dynamics and interactions. Below, we detail the state and control variables, along with the discretized system dynamics that form the foundation of our optimization framework. We adapt standard NMPC to the lane changing scenario where the stage cost incorporates multiple objectives including comfort, safety, and efficiency, while the constraints ensure collision avoidance through spatiotemporal safety corridors in (16). Specifically, the system state $\mathbf{z}_k = [s_0(k), v_0(k), a_0(k), s_2(k), v_2(k), a_2(k)]^\top$ contains both HV (subscript 0) and SV_2 (subscript 2) states, and the control input $\mathbf{u}_k = j_0(k)$ represents HV's jerk. The HV dynamics are discretized with the sampling time Δt and given as

$$\begin{bmatrix} s_0(k+1) \\ v_0(k+1) \\ a_0(k+1) \end{bmatrix} = \underbrace{\begin{bmatrix} 1 & \Delta t & \frac{\Delta t^2}{2} \\ 0 & 1 & \Delta t \\ 0 & 0 & 1 \end{bmatrix}}_{A} \begin{bmatrix} s_0(k) \\ v_0(k) \\ a_0(k) \end{bmatrix} + \underbrace{\begin{bmatrix} \frac{\Delta t^3}{6} \\ \frac{\Delta t^2}{2} \\ \Delta t \end{bmatrix}}_{B} j_0(k) \tag{23}$$

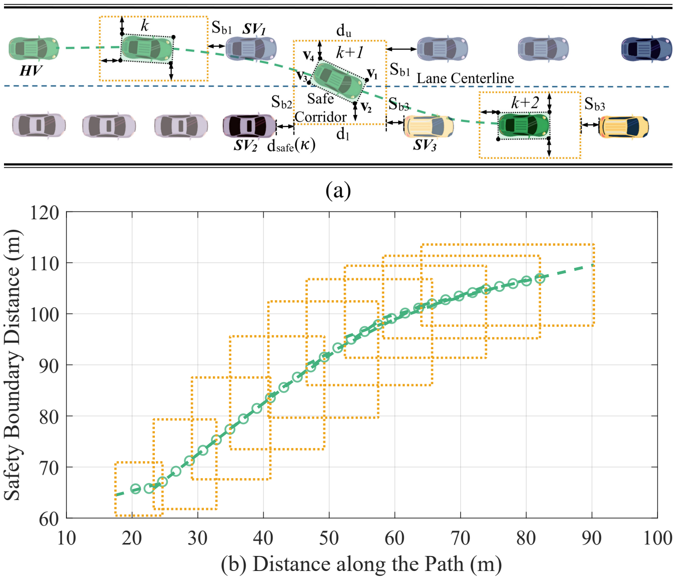

(a)

(b) Distance along the Path (m)

Fig. 6: Construction and regression of spatiotemporal safety corridors: (a) Safety corridors construction during lane change, with HV and SV_{1-3}; (b) Safety boundary regression using (20) where hollow circles represent the discrete boundary points from $\mathbf{S}_b$, dotted boxes represent their safety margins, and solid lines show the continuous boundary constraints at different k.

with state constraints $v_0(k) \in [v_{\min}, v_{\max}]$, $a_0(k) \in [a_{\min}, a_{\max}]$, and control input $j_0(k) \in [j_{\min}, j_{\max}]$. A and B are the system matrices obtained from the third-order Taylor expansion of the continuous dynamics in (1) around $\mathbf{z}_{\text{ref}}$.

To capture the uncertainty in SV_2's behavior during lane changing, we model its potential responses using a probabilistic framework. First, we define a set of possible scenarios as

$$\mathcal{S} = \{s_{\text{yield}}, s_{\text{constant}}, s_{\text{accelerate}}\} \tag{24}$$

where s_{yield} represents that the SV_2 yields to create space, s_{constant} represents maintaining current velocity, and $s_{\text{accelerate}}$ represents accelerating. The probability of the i-th scenario, $i \in \mathcal{S}$, is dynamically evaluated with a Boltzmann distribution based on the current traffic state as

$$p_i(k) = \frac{\exp(-\beta_i V_i(\mathbf{z}_k))}{\sum_{j \in \mathcal{S}} \exp(-\beta_j V_j(\mathbf{z}_k))}, \quad i \in \mathcal{S} \tag{25}$$

where β_i, $i \in \mathcal{S}$, are temperature parameters in HV's prediction model, representing the observed rationality of SV_2 in different scenarios. For the lane-change problem, these rationality parameters are determined based on SV_2's state information from the past few time steps. The cost function $V_i(\mathbf{z}_k)$ is defined as

$$V_i(\mathbf{z}_k) = \alpha_{1,i} d_{\text{rel}}(k) + \alpha_{2,i} |v_{\text{rel}}(k)| + \alpha_{3,i} |a_2(k)|$$

where $v_{\text{rel}}(k)$ is the relative velocity, and $d_{\text{rel}}(k)$ represents the relative distance between HV and SV_2. For each scenario $i \in \mathcal{S}$, we model SV_2's specific response by combining a deterministic IDM component with stochastic perturbations as

$$j_2^i(k) = j_{\text{IDM}}^i(k) + \epsilon_i(k) \tag{26}$$

with the scenario-specific IDM responses, given by

$$\begin{aligned} j_{\text{IDM}}^{\text{yield}}(k) &= -\eta_1(v_2(k) - v_{\text{des}}) - \eta_2(d_{\text{rel}}(k) - d_{\text{safe}}(k)) \\ j_{\text{IDM}}^{\text{constant}}(k) &= -\eta_3 a_2(k) \\ j_{\text{IDM}}^{\text{accelerate}}(k) &= \min(\eta_4(v_{\max} - v_2(k)), j_{\max}) \end{aligned}$$

where $\eta_1, ..., \eta_4$ are model parameters. $\epsilon_i(k) \sim \mathcal{N}(0, \sigma_i^2(k))$ captures scenario-specific uncertainties. The prediction uncertainty $\sigma^2(k)$ is adaptively set by

$$\sigma_i^2(k) = \alpha_i \cdot d_{\text{rel}}(k) + \beta_i \cdot |v_{\text{rel}}(k)| + \gamma_i \tag{27}$$

where v_{des} is the desired velocity, and $\{\alpha, \beta, \gamma\}$ are hyperparameters. The optimization problem is then formulated as

$$\begin{aligned} \min_{\mathbf{U}_k, \xi_j(k)} J(\mathbf{z}_k, \mathbf{U}_k, \xi_j(k)) &:= \sum_{i \in \mathcal{S}} p_i(k) \sum_{k=0}^{N-1} \big(w_{\text{com}} j_0(k)^2 \\ &+ w_{\text{saf}} J_{\text{saf}}^i(k) + w_{\text{eff}} J_{\text{eff}}(k) + w_{\text{fol}} J_{\text{fol}}(k) \big) \\ &+ \rho \sum_{k=0}^{N-1} \sum_{j=1}^{5} \xi_j(k)^2 + (\mathbf{z}_{k+N} - \mathbf{z}_{\text{ref}})^\top P (\mathbf{z}_{k+N} - \mathbf{z}_{\text{ref}}) \end{aligned} \tag{28}$$

$$\begin{aligned} \text{s.t. } & (23),\ \forall k \in [0, N-1],\ \mathbf{z}_{k+N} \in \mathcal{X}_f,\ j \in [1,5] \\ & s_{b1}(k) - s_0(k) - d_{\text{safe}}(\kappa) + \xi_1(k) \geq 0,\ (\text{for SV}_1) \\ & s_0(k) - s_{b2}^i(k) - d_{\text{safe}}(\kappa) + \xi_2(k) \geq 0,\ (\text{for SV}_2) \\ & s_{b3}(k) - s_0(k) - d_{\text{safe}}(\kappa) + \xi_3(k) \geq 0,\ (\text{for SV}_3) \\ & d_u(k) - d_0(k) + \xi_4(k) \geq 0,\ d_0(k) - d_l(k) + \xi_5(k) \geq 0 \\ & s_0(k+1) - s_0(k) \geq 0,\ \forall k \in [0, N-1] \end{aligned} \tag{29}$$

where $\mathbf{U}_k = \{\mathbf{u}_{k+i}\}_{i=0}^{N-1}$ represents the control sequence, and $\mathcal{X}_f$ denotes a control-invariant terminal set where the system can be stabilized around reference state $\mathbf{z}_{\text{ref}}$ through a terminal controller. The costs J_{eff}, J_{saf}^i, and J_{fol} are defined as

$$\begin{aligned} J_{\text{eff}}(k) &= (v_{\text{ref}} - v_0(k))^2 + \left(\frac{s_0(k) - s_s}{s_f - s_s} - \frac{k \Delta t}{T} \right)^2, \\ J_{\text{saf}}^i(k) &= \sum_{j=1}^{3} R_j(s_0(k), d_0(k)) + (s_0(k) - s_2^i(k) - d_{\text{safe}}(\kappa))^2, \\ J_{\text{fol}}(k) &= (s_0(k) - s_3(k) + d_{\text{safe}}(\kappa))^2 + (v_0(k) - v_3(k))^2. \end{aligned}$$

The safety cost J_{saf}^i and safety boundary s_{b2}^i depend on the predicted SV$_2$ states under each scenario $i \in \mathcal{S}$. $R_i(s_0(k), d_0(k))$ is the DRF as defined in (8), transformed to Frenet coordinates by using (9), (10), and (11). Here, SV$_2$'s predicted states based on the IDM model [6] are used in J_{saf} to consider its potential responses during lane changes. The safety constraints in (29) use regression-based safety boundaries $s_{b1}(k)$, $s_{b2}^i(k)$, and $s_{b3}(k)$ from (15) and (16), as shown in Fig. 6. With prediction horizon N, slack variables $\xi_j(k)$ allow minor constraint violations, penalized by weight ρ. The terminal set $\mathcal{X}_f$ and terminal cost term with weighting matrix P ensure convergence to $\mathbf{z}_{\text{ref}}$.

B. Solution Method for NMPC

To solve the optimization problem efficiently, we employ a sequential quadratic programming (SQP) method, which iteratively approximates the nonlinear problem by a sequence of quadratic subproblems.

Algorithm 2 Prediction-aware NMPC with contingency

```
Input: Initial states $\mathbf{z}_0$, DRF $R_i(x,y)$, $\mathbf{S}_b$, scenarios $\mathcal{S}$.
Set $N$, weights $w_{\text{com}}, w_{\text{saf}}, w_{\text{eff}}, w_{\text{fol}}$.
Set scenario parameters $\{\eta_1, ..., \eta_4\}$, $\{\alpha_i, \beta_i, \gamma_i\}_{i \in \mathcal{S}}$.
Initialize control sequence $\mathbf{U}_k^0$.
Compute LQR feedback gain $K$.
$j \leftarrow 0$.
while not converged do
    for $i \in \mathcal{S}$ do
        Calculate scenario probability $p_i(k)$ in (25).
        Predict SV$_2$ response $j_2^i(k)$ using (26).
        Update uncertainty $\sigma_i^2(k)$ in (27).
    end for
    // Solve QP subproblem at iteration $j$ //
    Compute scenario-specific Hessian $H_k^i$.
    Construct scenario-weighted $H_k = \sum_{i \in \mathcal{S}} p_i(k) H_k^i$.
    Compute scenario-dependent constraints in (31).
    Solve for $\Delta \mathbf{U}_k^*$ using SQP.
    // Update control sequence //
    Determine step size $\alpha_j$ via line search.
    Update: $\mathbf{U}_k^{j+1} = \mathbf{U}_k^j + \alpha_j \Delta \mathbf{U}_k^*$ in (32).
    // Check convergence //
    Calculate weighted cost reduction $\Delta J_k$ in (33)
    Evaluate scenario-wise primal-dual feasibility
    $j \leftarrow j + 1$.
end while
// Ensure stability and recursive feasibility //
Verify terminal states: $\mathbf{z}_{k+N}^i \in \mathcal{X}_f, \forall i \in \mathcal{S}$.
Apply terminal controller $\kappa_f(\mathbf{z}_k)$.
Return: Optimal control sequence $\mathbf{U}_k^*$
```

1) Lagrangian Formulation: The augmented Lagrangian incorporates both system dynamics and safety constraints:

$$\begin{aligned} \mathcal{L}(\mathbf{z}_k, \mathbf{U}_k, \xi_j(k), \lambda_k, \mu_k) &= \sum_{i \in \mathcal{S}, j \in [1,5]} p_i(k) J(\mathbf{z}_k, \mathbf{U}_k, \xi_j(k)) \\ &+ \sum_{k=0}^{N-1} \mu_k^\top \underbrace{g(\mathbf{z}_k, \mathbf{u}_k, \xi_j(k))}_{\text{safety constraints}} + \lambda_k^\top \underbrace{(A\mathbf{z}_k + B\mathbf{u}_k - \mathbf{z}_{k+1})}_{\text{dynamics constraints}} \\ \text{s.t.}\quad & \mathbf{z}_k \in \mathcal{Z},\ \mathbf{u}_k \in \mathcal{U},\ \mathbf{z}_{k+1} = A\mathbf{z}_k + B\mathbf{u}_k,\ \mathbf{z}_{k+N} \in \mathcal{X}_f \end{aligned} \tag{30}$$

where $g(\mathbf{z}_k, \mathbf{u}_k, \xi_j(k))$ represents the safety constraints in (29). The Lagrange multipliers $\lambda_k \in \mathbb{R}^3$ and $\mu_k \in \mathbb{R}^5$ indicate the sensitivity of the cost function to dynamics and safety constraint violations, respectively.

2) SQP Method: At each iteration j, we solve the following scenario-weighted quadratic approximation:

$$\begin{aligned} \min_{\Delta \mathbf{U}_k} \sum_{i \in \mathcal{S}} & p_i(k) \left(\frac{1}{2} \Delta \mathbf{U}_k^\top H_k^i \Delta \mathbf{U}_k + {g_k^i}^\top \Delta \mathbf{U}_k \right) \\ & + \frac{1}{2} \Delta \mathbf{z}_{k+N}^\top P \Delta \mathbf{z}_{k+N} \\ \text{s.t.}\quad & C_k \Delta \mathbf{U}_k + c_k = 0,\ D_k^i \Delta \mathbf{U}_k + d_k^i \leq 0,\ \forall i \in \mathcal{S}, \\ & \mathbf{z}_{k+N}^i + \Delta \mathbf{z}_{k+N}^i \in \mathcal{X}_f,\ \forall i \in \mathcal{S} \end{aligned} \tag{31}$$

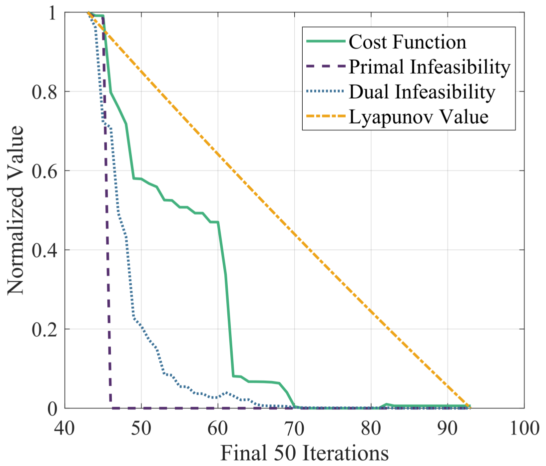

Fig. 7: Convergence analysis of the proposed method.

where, for each scenario $i \in \mathcal{S}$, we have

$$H_k^i{=}\nabla^2_{\mathbf{U}_k\mathbf{U}_k}\mathcal{L}_i(\mathbf{U}_k^j{,}\lambda^j{,}\mu^j),\ g_k^i{=}\nabla_{\mathbf{U}_k}\mathcal{L}_i(\mathbf{U}_k^j{,}\lambda^j{,}\mu^j),$$
$$C_k{=}\nabla_{\mathbf{U}_k}h(\mathbf{U}_k^j),\ \Delta\mathbf{z}_{k+N}^i = \nabla_{\mathbf{U}_k}\mathbf{z}_{k+N}^i(\mathbf{U}_k^j)\Delta\mathbf{U}_k,$$
$$D_k^i{=}\nabla_{\mathbf{U}_k}g_i(\mathbf{U}_k^j),\ h(\mathbf{U}_k^j) = A\mathbf{z}_k + B\mathbf{u}_k - \mathbf{z}_{k+1} = 0.$$

The scenario-specific Hessian matrix H_k^i and gradient g_k^i incorporate both the nominal cost and the uncertainty terms associated with scenario i's prediction model, where H_k^i represents the second-order derivative and g_k^i the first-order derivative of the scenario-dependent Lagrangian $\mathcal{L}_i$ with respect to $\mathbf{U}_k$. While C_k represents the gradient of the HV dynamics constraints $h(\mathbf{U}_k^j)$, D_k^i captures the gradients of safety constraints that depend on the predicted states of SV$_2$ under scenario i. The control input sequence is updated by

$$\mathbf{U}_k^{j+1} = \mathbf{U}_k^j + \alpha_j \Delta\mathbf{U}_k^* \tag{32}$$

where $\Delta\mathbf{U}_k^*$ is the optimal solution to the scenario-weighted quadratic subproblem. The step size α_j is determined by the weighted Armijo line search condition:

$$\sum_{i\in\mathcal{S}} p_i(k) J_i(\mathbf{U}_k^j + \alpha_j\Delta\mathbf{U}_k^*) \le \sum_{i\in\mathcal{S}} p_i(k) J_i(\mathbf{U}_k^j) + c\alpha_j \nabla J(\mathbf{U}_k^j)^\top \Delta\mathbf{U}_k^*$$

where $c \in (0,1)$ is a constant parameter. The whole procedure of contingency NMPC is illustrated in Algorithm 2.

3) Convergence Analysis of SQP Method: The convergence properties of the proposed method are analyzed from three aspects: cost function convergence, primal-dual feasibility, and Lyapunov stability, as shown in Fig. 7. The convergence rate is characterized by the following metrics:

$$\begin{aligned}
&\text{Cost reduction: } \Delta J_k = \Big|\sum_{i\in\mathcal{S}} p_i(k)[J_i(\mathbf{z}_k,\mathbf{U}_k) - J_i(\mathbf{z}_k,\mathbf{U}_{k-1})]\Big| \\
&\text{Primal feasibility: } \|A\mathbf{z}_k + B\mathbf{u}_k - \mathbf{z}_{k+1}\|_2 \\
&\text{Dual feasibility: } \Big\|\sum_{i\in\mathcal{S}} p_i(k)\nabla_{\mathbf{U}_k}\mathcal{L}_i(\mathbf{U}_k^j,\lambda_k^j,\mu_k^j)\Big\|_2
\end{aligned} \tag{33}$$

As shown in Fig. 7, all metrics exhibit consistent convergence behavior: the cost function value (green line) initially descends rapidly, followed by steady convergence to the optimal value, demonstrating the effectiveness of the scenario-weighted SQP updates. The primal and dual infeasibility measures (purple and blue lines) decrease monotonically, confirming that the solution increasingly satisfies the KKT conditions. The Lyapunov value (yellow line) exhibits a linear decay rate, supporting the practical convergence properties of the algorithm.

C. Practical Convergence Analysis and Terminal Control

The proposed contingency NMPC approach introduces unique challenges for stability analysis due to its scenario-based predictions and time-varying probabilities. Our formulation extends standard NMPC through scenario-weighted cost functions and the incorporation of multiple predicted behaviors of SV$_2$, making theoretical stability proof particularly challenging. Therefore, we focus on establishing practical stability through rigorous analysis and numerical validation.

Upon completing the lane changing maneuver, the vehicle's motion will be either car-following or cruising in the target lane, under both of which the operating points vary within a small range around the equilibrium state. This allows us to approximate the system dynamics using a linear model. The terminal set $\mathcal{X}_f$ maintains three essential constraints:

$$\begin{aligned}
&s_{b3}(k) - s_0(k) - d_{\text{safe}}(\kappa) \ge 0 && \text{(for SV}_3\text{)} \\
&d_u(k) - d_0(k) \ge 0,\ d_0(k) - d_l(k) \ge 0 && \text{(lateral bounds)} \\
&s_0(k+1) - s_0(k) \ge 0,\ \forall k \in [0, N-1] && \text{(monotonicity)}
\end{aligned}$$

where the longitudinal safety constraint with SV$_3$ ensures safe car-following behavior in the target lane, while lateral bounds maintain stable lane-keeping. Within this terminal region, the system dynamics can be approximated by a linear model, allowing for the design of a stabilizing terminal controller:

$$\kappa_f(\mathbf{z}_k) = K(\mathbf{z}_k - \mathbf{z}_{\text{ref}}) + \mathbf{u}_{\text{ref}} \tag{34}$$

where $K \in \mathbb{R}^{1\times3}$ is the feedback gain matrix obtained through the LQR technique [38], and $\mathbf{z}_{\text{ref}}$ represents either car-following with a safe distance or cruising at desired velocity v_{ref}, depending on the presence of a preceding vehicle SV$_3$.

To handle SV uncertainties, the NMPC uses scenario-based predictions and slack variables, ensuring adaptive, feasible control that balances safety and performance. Fig. 7 shows consistent convergence of the scenario-weighted cost and constraints, with control inputs staying within limits. The steady decline of the Lyapunov function indicates smooth, stable responses. While theoretical stability with time-varying scenario probabilities is challenging, the results demonstrate safe, efficient lane changes in dynamic settings. In dynamic traffic, our contingency-aware approach ensures recursive feasibility via: 1) slack variables $\xi_j(k)$ to allow minor, penalized constraint violations; 2) scenario-weighted optimization to handle varied traffic evolutions; and 3) terminal constraints for safe fallback states. Though complex cases may raise iterations to 230 (vs. 90–150 typically), computation remains real-time feasible. Like human decision-making [39], our method considers multiple SV responses, but offers greater interpretability and explicit safety guarantees.

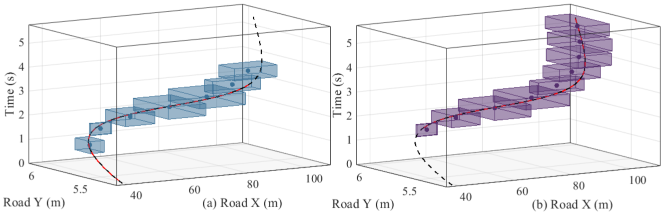

Fig. 8: Spatiotemporal corridors for HV during lane change. (a) shows the spatiotemporal corridor constructed for the lead vehicle in the original lane before lane change, (b) shows the spatiotemporal corridor constructed for the rear vehicle in the target lane. The dashed line represents the trajectory of HV.

TABLE II:
COMPARISON OF ALGORITHM PERFORMANCES IN CASE 1.

Methods	x_{a} (m/s^2)	y_{a} (m/s^2)	x_{j} (m/s^3)	y_{j} (m/s^3)	T (s)
Ours	$\mathbf{0.0642}$	$\mathbf{0.0008}$	0.0911	0.0061	$\mathbf{4.84 \pm 0.03}$
SQP	-1.3585	-0.0879	0.1119	0.0091	5.31 ± 0.04
A_S	-0.1512	0.0092	$\mathbf{0.0011}$	$\mathbf{0.0008}$	6.62 ± 0.05
GA	-0.1860	-0.0158	0.2005	0.0092	6.63 ± 0.05

x_{a}, y_{a}: average longitudinal and lateral accelerations; x_{j}, y_{j}: average longitudinal and lateral jerks; T: average lane changing time.

VI. SIMULATION RESULTS

Simulations are conducted in MATLAB 2023b to evaluate the proposed approach for safe and efficient autonomous driving in various lane changing scenarios. We make comparison between the proposed SQP and several advanced optimization algorithms including SQP [40], Active Set (A_S) method [41], and Genetic Algorithm (GA) [42]. These baseline methods represent diverse optimization paradigms commonly applied in trajectory planning. They were chosen after preliminary experiments where other algorithms (e.g., Differential Evolution and Particle Swarm Optimization) frequently failed to find feasible solutions under the strict lane-changing safety constraints.

Our experiments target a core lane-changing pattern: HV coordination with three key SVs—consistent across traffic complexities. Spatiotemporal safety corridors (Fig. 8) adapt to vehicle setups and densities, ensuring robust safety. The contingency-aware framework handles traffic randomness via scenario-based predictions with adaptive uncertainty (25), and (27). Traffic density is tested by varying gaps, with the DRF adjusting safety margins based on proximity and relative speed.

Case 1: **Lane Changing Performance on Highway.** This case considers a two-lane highway scenario where the HV changes lanes while accounting for three SVs positioned across both lanes, requiring careful coordination.

Figure 8 illustrates our spatiotemporal safety corridor construction during lane changing. In Fig. 8(a), a blue spatiotemporal safety corridor is initially constructed for SV$_1$ in the original lane, deactiving once the HV crosses the lane centerline. In Fig. 8(b), a purple safety corridor is established for SV$_2$ when HV approaches the target lane. Dashed trajectories within these corridors show the paths that satisfy safety constraints while enabling smooth lane transitions.

The comparative performance analysis presented in Fig. 9 demonstrates the superiority of our approach under zero acceleration conditions for SV$_2$ ($a_r = 0$). Fig. 9(a) visualizes vehicle positions from time $0.00\ \mathrm{s} - 5.60\ \mathrm{s}$ and the DRF at 3.06 s, where the color gradient indicates varying risk levels. The trajectory comparison in Fig. 9(b) reveals that our method generates significantly smoother paths with more consistent curvature compared to the baseline approaches. The longitudinal velocity profile shown in Fig. 9(c) demonstrates remarkable stability, maintaining speeds between $14 - 16\ \mathrm{m/s}$ throughout the maneuver. The lateral velocity profile in Fig. 9(d) shows that our method always maintains stability during the lane change process, while Fig. 9(e) shows well-contained overall jerk values within $\pm 0.3\ \mathrm{m/s^3}$, indicating superior comfort characteristics during the lane change execution.

The statistical performance metrics illustrated in Fig. 10 through box plots further validate efficacy of our algorithm. The velocity distribution shows higher median values with notably smaller variances than baselines, while acceleration remains predominantly within $\pm 1\ \mathrm{m/s^2}$. The jerk distribution centers near zero, indicating smoother control. Figure 11 shows that our approach consistently maintains optimal safety gaps with all SVs, with a reliable $15\ \mathrm{m}$ spacing from SV$_1$ and systematic distance management with SV$_2$ and SV$_3$.

Table II provides quantitative validation of our method's performance across key metrics. Our approach demonstrates superior trajectory smoothness and stability, with up to 95% reductions in accelerations (95.3% reduction from $|-1.3585|$ to $|0.0642|\ \mathrm{m/s^2}$ longitudinally, and 99.1% from $|-0.0879|$ to $|0.0008|\ \mathrm{m/s^2}$ laterally) compared to baseline methods. Additionally, our method achieves a highly consistent lane change time of $4.84 \pm 0.03\ \mathrm{s}$, showcasing both efficiency and adherence to safety constraints. While the A_S method achieves comparable jerk minimization, it lacks stability in acceleration control.

Despite sharing identical mathematical constraint formulations, the different optimization algorithms yield varying performance as shown in Table II due to several factors. First, each algorithm employs different searching strategies that traverse the solution space differently. Our SQP-based approach utilizes scenario-weighted Hessian matrices in (31), enabling more effective navigation of the highly nonlinear cost landscape. In contrast, the baseline SQP focuses solely on the current state without incorporating scenario probabilities, while A_S prioritizes constraint satisfaction over optimality, and GA's stochastic nature leads to suboptimal convergence in this context. Second, our method's dynamic risk field integration provides gradient information that guides optimization more effectively than discrete constraints alone, allowing for smoother trajectories with smaller acceleration variations. Third, the spatiotemporal corridor construction enables phase-dependent constraint activation, reducing unnecessary restrictions during optimization. These advantages collectively contribute to our method's superior acceleration control and efficiency, as evidenced by the 95% reduction in longitudinal acceleration and 27% decrease in lane-changing time compared to baseline methods.

Case 2: **Performance Under Different SV$_2$ Uncertainties.** To validate our prediction-aware NMPC with contingency

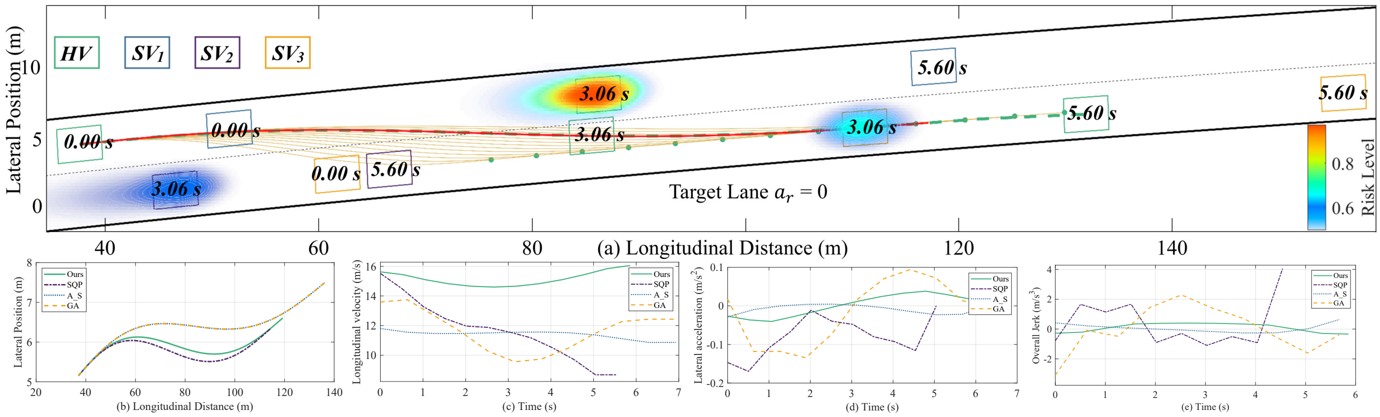

Fig. 9: Comparison of our algorithm's performance on the road with different algorithmic metrics under the condition of the SV_2 acceleration $a_r = 0$. (a) DRF and vehicle positions at different times in Cartesian coordinates, with lane change occurring at $T = 3.06$ s. (b) Comparison of lateral position Y versus longitudinal position X in Cartesian coordinates. (c) Longitudinal velocity comparison over time. (d) Lateral velocity comparison over time. (e) Overall jerk comparison over time.

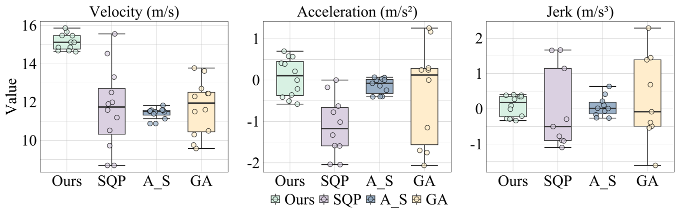

Fig. 10: Comparison of overall performances.

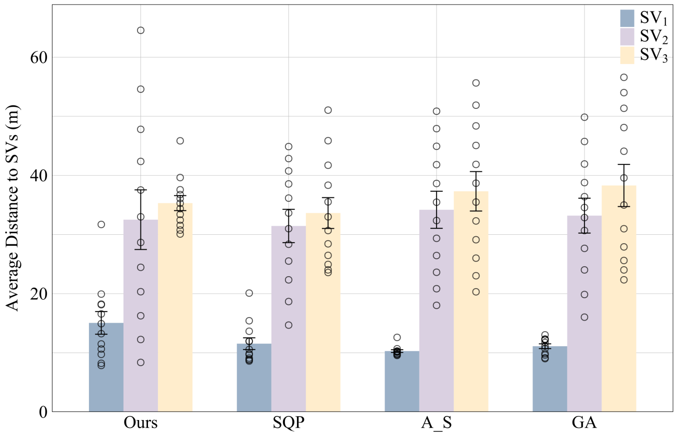

Fig. 11: Algorithmic comparison of average distance to SVs.

handling, we tested its adaptability across varying SV_2 accelerations while balancing safety, efficiency, and comfort. As shown in Fig. 12, our algorithm leverages the scenario-specific prediction model in (26) to identify the more aggressive response patterns of SV_2 with acceleration $a_r = 3\ \mathrm{m/s^2}$, enabling more efficient trajectory planning that completes the lane changing in 4.04 s versus 5.16 s when $a_r = 2\ \mathrm{m/s^2}$. The velocity profiles in Figs. 12(b)(c) reveal how our scenario-weighted optimization strategy in (31) systematically adapts to different SV_2 capabilities. Under higher SV_2 acceleration ($a_r = 3\ \mathrm{m/s^2}$), the algorithm prioritizes shorter paths while maintaining safety bounds through the adaptive constraints in (29), demonstrating the framework's ability to balance multiple objectives based on predicted vehicle responses.

TABLE III:
COMPARISON OF ALGORITHM PERFORMANCES IN CASE 2.

Scenarios	x_a ($\mathrm{m/s^2}$)	y_a ($\mathrm{m/s^2}$)	x_j ($\mathrm{m/s^3}$)	y_j ($\mathrm{m/s^3}$)	T (s)
$a_r = 0$	0.0642	0.0008	0.0911	0.0061	4.84 ± 0.03
$a_r = 1$	-0.1665	-0.0142	0.2425	0.0133	4.22 ± 0.04
$a_r = 2$	-0.1096	0.0110	0.2307	0.0127	4.64 ± 0.04
$a_r = 3$	-0.0250	-0.0063	0.2659	0.0155	4.04 ± 0.03

$x_\mathrm{a}, y_\mathrm{a}$: average longitudinal and lateral accelerations; $x_\mathrm{j}, y_\mathrm{j}$: average longitudinal and lateral jerks; T: average lane changing time.

The statistical analysis in Fig. 13 quantifies the performance of our contingency handling mechanism. The systematic increase in median velocity with higher a_r values (from $12.5\ \mathrm{m/s}$ to $15\ \mathrm{m/s}$ at different a_r) demonstrates how our contingency framework enables more efficient trajectories when conditions permit. Through optimizing the scenario-weighted cost function, both acceleration and jerk profiles remain well-controlled ($\pm 1.0\ \mathrm{m/s^2}$ and $\pm 0.5\ \mathrm{m/s^3}$ respectively) across all scenarios, indicating that the improved efficiency does not compromise comfort constraints.

Figure 14 demonstrates our framework's adaptive safety management across traffic scenarios. For constant-velocity cases ($a_r = 0\ \mathrm{m/s^2}$), the algorithm maintains conservative trajectories with larger safety margins (30 m to SV_2) and lower curvature by prioritizing the 'yield' scenario in (25). For higher accelerations ($a_r = 3\ \mathrm{m/s^2}$), it adjusts safety constraints to enable efficient trajectories with robust safety.

The quantitative analysis in Table III further validates our framework's performance across varying acceleration scenarios. At $a_r = 0\ \mathrm{m/s^2}$, the algorithm achieves minimal longitudinal and lateral accelerations ($a_x = 0.1254\ \mathrm{m/s^2}$, $a_y = 0.0876\ \mathrm{m/s^2}$). As a_r increases to $3\ \mathrm{m/s^2}$, the framework maintains stability while allowing slightly higher dynamics ($x_j = 0.2659\ \mathrm{m/s^3}$), demonstrating its ability to balance efficiency and safety through prediction-aware optimization. The consistent lane changing completion times (averaging 5 s) across conditions verify the framework's reliable performance under different interaction scenarios.

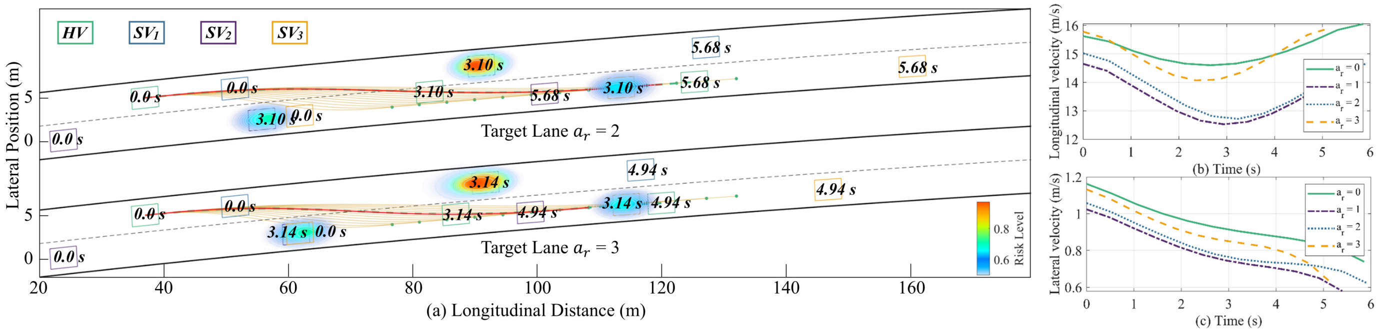

Fig. 12: Comparison of DRF and vehicle trajectories under different target lane rear vehicle accelerations. (a) shows DRF and vehicle positions at different times in Cartesian coordinates, with lane changing occurring at $T \approx 3$ s. (b) and (c) show the longitudinal and lateral velocities over time for $a_r = 0, 1, 2, 3\ \mathrm{m/s^2}$, respectively.

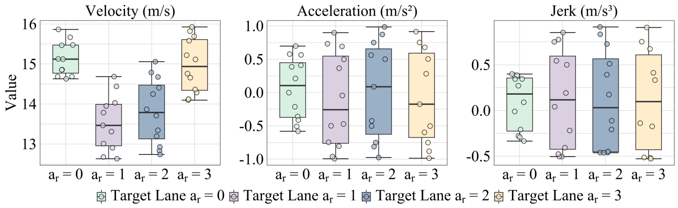

Fig. 13: Overall performance analysis for different a_r.

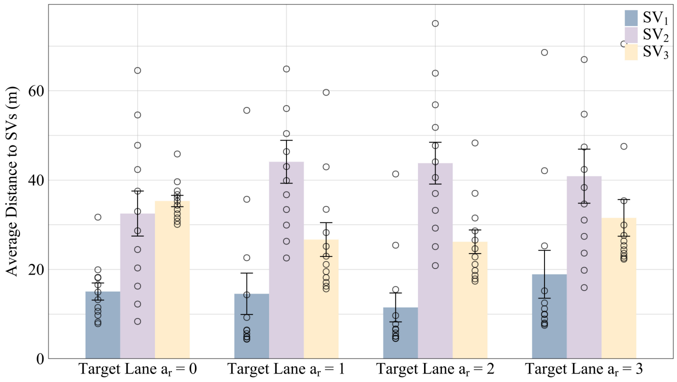

Fig. 14: Average distance to SVs for varying a_r.

TABLE IV:
COMPUTATIONAL EFFICIENCY COMPARISON OF DIFFERENT OPTIMIZATION METHODS.

Methods	Computation Time (ms)			Iter. Conv.
	Low	Mid.	High	
Ours	42.3 ± 3.8	68.5 ± 5.2	94.7 ± 7.1	133 ± 19
SQP	58.7 ± 4.5	87.4 ± 6.3	126.3 ± 8.9	187 ± 31
A_S	72.6 ± 5.8	108.4 ± 7.2	154.2 ± 10.6	143 ± 38
GA	285.3 ± 18.7	412.5 ± 24.6	598.7 ± 35.2	242 ± 54

Low, Mid., and High denote optimization convergence tolerance settings of $\delta = 10^{-3}$, $\delta = 10^{-4}$, and $\delta = 10^{-6}$, respectively.

Table III demonstrates how our optimization framework adapts to different SV$_2$ acceleration scenarios while maintaining identical constraint structures. Although the mathematical formulation of constraints remains consistent across scenarios, the actual optimization landscape varies significantly due to three key factors. First, different a_r values directly alter the prediction model in (26), changing the likelihood distribution $p_i(k)$ over possible scenarios through (25). For higher accelerations (e.g., $a_r = 3\ \mathrm{m/s^2}$), the algorithm assigns greater probability to the "accelerate" scenario, effectively reshaping the scenario-weighted objective function. Second, the adaptive prediction uncertainty $\sigma_i^2(k)$ in (27) scales with relative dynamics, creating scenario-specific confidence intervals that influence both constraint boundaries and cost evaluation. Third, while constraint structures remain identical, their numerical values evolve as safety boundaries adapt to changing vehicle dynamics through $s_{b2}^i(k)$ in (29), resulting in different feasible regions for each a_r value.

The results demonstrate that our contingency-aware NMPC enables safer, more efficient lane changes through three key mechanisms: (a) The scenario-based prediction model enables proactive trajectory adjustment based on anticipated vehicle responses. (b) The scenario-weighted optimization allows dynamic safety margin adaptation based on predicted behaviors. (c) The integrated handling of multiple contingencies ensures controlled comfort metrics even during dynamic maneuvers.

***Case 3:* Computational Efficiency Analysis.** To evaluate deployment feasibility of our framework in real-world AVs, we tested computational efficiency across optimization methods and accuracy settings on an Intel i5-12600KF CPU, reflecting typical automotive hardware.

The results in Table IV reveal that our method has superior efficiency over the baselines, requiring 22% less computation time than standard SQP, 37% less than A_S, and 83% less than GA at medium accuracy settings. This advantage comes from the scenario-weighted design and fast convergence, as shown in Fig. 7, where the cost drops quickly in early iterations. The table shows a 28% time reduction from high to medium accuracy with minimal impact ($< 3\%$ increase in jerk), and a further 38% cut at low accuracy with acceptable trade-offs. The average 68.5 ms runtime at medium accuracy meets the 10 Hz control update rate, supporting real-world feasibility.

***Case 4:* Discussion and Limitations.** The quantitative results show our contingency-aware framework outperforms baseline methods. As evidenced in Table II, our method achieves up to 95% reductions. The framework also delivers a 27% reduction in lane-changing completion time (4.84 s versus 6.3 s for baseline methods), while maintaining consistent safety margins as illustrated in Fig. 11. Furthermore, our adaptability analysis across varying SV$_2$ acceleration scenarios

(Table III) confirms the robust performance of the prediction-aware planning approach in dynamic traffic environments. Notably, as SV_2 acceleration increases from 0 to $3\ \mathrm{m/s^2}$, our framework maintains acceleration values within $\pm 0.17\ \mathrm{m/s^2}$ longitudinally and $\pm 0.1\ \mathrm{m/s^2}$ laterally, while simultaneously reducing lane-changing time from $4.84\ \mathrm{s}$ to $4.04\ \mathrm{s}$, a 16.5% efficiency improvement. This shows the framework adapts to traffic changes while preserving comfort and safety.

Our performance gains result from the synergy of four key components. First, the DRF offers smooth, direction-aware risk gradients that support stable trajectories without the oscillations seen in traditional potential fields. Second, spatiotemporal safety corridors with regression-based boundaries simplify constraint handling and adapt during lane changes using a phase function $\phi(k)$. Third, the contingency-aware approach incorporates scenario probabilities $p_i(k)$, enabling smoother optimization across multiple SV responses and reducing sharp trajectory shifts. Lastly, recursive feasibility mechanisms—slack variables $\xi_j(k)$ and a terminal controller—add flexibility, preventing abrupt control actions under tight constraints. Together, these features ensure safety while minimizing acceleration and jerk.

Despite its advantages, the framework has limitations. In dense traffic with minimal gaps, the solution space narrows, leading to more conservative actions or higher computation. Abrupt SV maneuvers outside the modeled scenarios in $\mathcal{S}$ may briefly lower prediction accuracy until $p_i(k)$ adjusts. Expanding scenario diversity and using adaptive safety margins could help, though at a computational cost. Nevertheless, the consistent performance demonstrated across multiple evaluation scenarios validates the framework's effectiveness for typical highway lane-changing maneuvers.

VII. CONCLUSION

This paper presents a comprehensive framework for autonomous lane changing that prioritizes safety, comfort, and efficiency in dynamic traffic. It features a DRF for inter-vehicle risk assessment, a Spatiotemporal Safety Corridor for efficient constraint management, and a prediction-aware NMPC that anticipates surrounding vehicles' responses. Using regression-based boundaries and an IDM-based model, the NMPC adapts lane changes based on rear vehicle behavior, balancing efficiency and conservatism while maintaining safety margins. Simulations confirm stability, with smooth trajectories and minimal accelerations, balancing efficiency, safety, comfort. Future work will explore complex traffic scenarios with learning-based predictions, develop stability analysis tools for NMPC with scenario-based forecasts, and validate real-time performance using high-fidelity simulators like CARLA and experimental setups.

REFERENCES

[1] C. Badue, R. Guidolini, R. Carneiro, *et al.*, "Self-driving cars: A survey," *Expert Syst. Appl.*, vol. 165, no. 113816, p. 113816, 2021.

[2] P. Scheffe, M. V. A. Pedrosa, K. Flaßkamp, and B. Alrifaee, "Receding horizon control using graph search for multi-agent trajectory planning," *IEEE Trans. Control Syst. Technol.*, vol. 31, no. 3, pp. 1092–1105, 2023.

[3] Y. Yan, D. Han, Q. Zhang, J. Wang, D. Pi, D. Chu, and G. Yin, "Event-triggered personalized driving based on passenger's subjective risk evaluation," *IEEE Trans. Intell. Transp. Syst.*, vol. 26, no. 2, pp. 1982–1998, 2025.

[4] G. Chen, Y. Zhang, and X. Li, "Attention-based highway safety planner for autonomous driving via deep reinforcement learning," *IEEE Trans. Veh. Technol.*, vol. 73, no. 1, pp. 162–175, 2024.

[5] Y. Yan, C. Zhang, P. Xue, *et al.*, "Research on hierarchical motion control of corner module configuration intelligent electric vehicle," *Chin. J. Mech. Eng.*, vol. 38, p. 23, 2025.

[6] X. Hu, Z. Zheng, D. Chen, and J. Sun, "Autonomous vehicle's impact on traffic: Empirical evidence from Waymo open dataset and implications from modelling," *IEEE Trans. Intell. Transp. Syst.*, vol. 24, no. 6, pp. 6711–6724, 2023.

[7] Z. Tian, D. Zhao, Z. Lin, D. Flynn, W. Zhao, and D. Tian, "Balanced reward-inspired reinforcement learning for autonomous vehicle racing," in *Proc. L4DC*, 2024, pp. 628–640.

[8] D. Li, J. Zhang, and G. Liu, "Autonomous driving decision algorithm for complex multi-vehicle interactions: An efficient approach based on global sorting and local gaming," *IEEE Trans. Intell. Transp. Syst.*, vol. 25, no. 7, pp. 6927–6937, 2024.

[9] M. Lv, Y. Li, H. Liang, B. Sun, C. Yang, and W. Gui, "A spatial–temporal variational graph attention autoencoder using interactive information for fault detection in complex industrial processes," *IEEE Trans. Neural Netw. Learn. Syst.*, vol. 35, no. 3, pp. 3062–3076, 2024.

[10] J. Zhang, S.-C. Chai, B.-H. Zhang, and G.-P. Liu, "Distributed model-free sliding-mode predictive control of discrete-time second-order nonlinear multiagent systems with delays," *IEEE Trans. Cybern.*, vol. 52, no. 11, pp. 12 403–12 413, 2022.

[11] J. Wurts, J. L. Stein, and T. Ersal, "Design for real-time nonlinear model predictive control with application to collision imminent steering," *IEEE Trans. Control Syst. Technol.*, vol. 30, no. 6, pp. 2450–2465, 2022.

[12] P. Zhou, X. Sun, and T. Chai, "Enhanced NMPC for stochastic dynamic systems driven by control error compensation with entropy optimization," *IEEE Trans. Control Syst. Technol.*, vol. 3, no. 5, pp. 17–30, 2023.

[13] T. M. Rajeh, Z. Luo, M. H. Javed, F. Alhaek, and T. Li, "A clustering-based multi-agent reinforcement learning framework for finer-grained taxi dispatching," *IEEE Trans. Intell. Transp. Syst.*, vol. 25, no. 9, pp. 11 269–11 281, 2024.

[14] P. Ladosz, M. Mammadov, H. Shin, W. Shin, and H. Oh, "Autonomous landing on a moving platform using vision-based deep reinforcement learning," *IEEE Robot. Autom. Lett.*, vol. 9, no. 5, pp. 4575–4582, 2024.

[15] Z. Tian *et al.*, "Efficient and balanced exploration-driven decision making for autonomous racing using local information," *IEEE Trans. on Intell. Veh.*, pp. 1–17, 2024.

[16] Z. Lin *et al.*, "A conflicts-free, speed-lossless kan-based reinforcement learning decision system for interactive driving in roundabouts," *IEEE Trans. Intell. Transp. Syst.*, vol. 25, pp. 1–14, 2025.

[17] C. Zhao *et al.*, "A novel direct trajectory planning approach based on generative adversarial networks and rapidly-exploring random tree," *IEEE Trans. Intell. Transp. Syst.*, vol. 23, no. 10, pp. 910–921, 2022.

[18] P. Li, C. Zhi, and W. Li, "An algorithm to solve heterogeneous vehicle routing problem with second trip," *IEEE Access*, vol. 9, pp. 12 241–12 255, 2021.

[19] Z. Lin, Z. Tian, Q. Zhang, H. Zhuang, and J. Lan, "Enhanced visual slam for collision-free driving with lightweight autonomous cars," *Sensors*, vol. 24, no. 19, p. 6258, 2024.

[20] C.-K. Ho and C.-T. King, "LAC-RRT: Constrained rapidly-exploring random tree with configuration transfer models for motion planning," *IEEE Access*, vol. 11, pp. 97654–97663, 2023.

[21] P. Bhattacharya and M. Gavrilova, "Voronoi diagram in optimal path planning," in *Proc. ISVD*, 2007, pp. 38–47.

[22] W. Chi, Z. Ding, J. Wang, G. Chen, and L. Sun, "A generalized Voronoi diagram-based efficient heuristic path planning method for RRTs in mobile robots," *IEEE Trans. Indus. Electron.*, vol. 69, no. 5, pp. 4926–4937, 2022.

[23] Y. Gao, D. Li, Z. Sui, and Y. Tian, "Trajectory planning and tracking control of autonomous vehicles based on improved artificial potential field," *IEEE Trans. Veh. Technol.*, vol. 73, no. 9, pp. 12468–12483, 2024.

[24] R. Szczepanski, "Safe artificial potential field: Novel local path planning algorithm maintaining safe distance from obstacles," *IEEE Robot. Autom. Lett.*, vol. 8, no. 8, pp. 4823–4830, 2023.

[25] W. Zhong, X. Huang, Y. Wu, R. Yu, and J. Kang, "Decentralized energy management for wireless power transfer assisted platoon autonomous driving: A leader-to-follower approach," *IEEE Trans. Green Commun. Netw.*, vol. 6, no. 4, pp. 2073–2083, 2022.

[26] D.-J. Kim, Y.-W. Jeong, and C.-C. Chung, "Lateral vehicle trajectory planning using a model predictive control scheme for an automated perpendicular parking system," *IEEE Trans. Indus. Electron.*, vol. 70, no. 2, pp. 1820–1829, 2023.

[27] D. Lenz, T. Kessler, and A. Knoll, "Tactical cooperative planning for autonomous highway driving using Monte-Carlo tree search," in *Proc. IV*, 2016, pp. 447–453.

[28] F. Altché and A. de La Fortelle, "Partitioning of the free space-time for on-road navigation of autonomous ground vehicles," in *Proc. CDC*, 2017, pp. 2126–2133.

[29] M. Wang, Z. Wang, L. Zhang, and D. Dorrell, "Speed planning for autonomous driving in dynamic urban driving scenarios," in *Proc. ECCE*, 2020, pp. 1462–1468.

[30] T. Ravi and D. Siddharth, "Handover count based map estimation of velocity with prior distribution approximated via NGSIM dataset," *IEEE Trans. Intell. Transp. Syst.*, vol. 23, no. 5, pp. 4352–4361, 2022.

[31] X. Shi and X. Li, "Empirical study on car-following characteristics of commercial automated vehicles with different headway settings," *Transp. Res. Part C: Emerg. Technol.*, vol. 128, p. 103134, 2021.

[32] K. Xu, C. G. Cassandras, and W. Xiao, "Decentralized time and energy-optimal control of connected and automated vehicles in a roundabout with safety and comfort guarantees," *IEEE Trans. Intell. Transp. Syst.*, vol. 24, no. 1, pp. 657–672, 2023.

[33] R. Chai, Y. Guo, Z. Zuo, K. Chen, H.-S. Shin, and A. Tsourdos, "Cooperative motion planning and control for aerial-ground autonomous systems: Methods and applications," *Prog. Aerosp. Sci.*, vol. 146, p. 101005, 2024.

[34] T. Xia, H. Chen, J. Yang, and Z. Guo, "Geometric field model of driver's perceived risk for safe and human-like trajectory planning," *Transp. Res. Part C: Emerg. Technol.*, vol. 159, p. 104470, 2024.

[35] M. Wang, L. Zhang, Z. Zhang, and Z. Wang, "An enabling decision-making scheme by considering trajectory prediction and motion uncertainty," *IEEE Trans. Intell. Veh.*, vol. 9, no. 5, pp. 4946–4961, 2024.

[36] H. Guan, Q. Meng, and X. Chen, "Dynamic lane management for emerging mixed traffic with semi-autonomous vehicles," *Transp. Res. Part C: Emerg. Technol.*, vol. 170, p. 104914, 2025.

[37] J. Hu, Y. Zhang, and S. Rakheja, "Adaptive lane change trajectory planning scheme for autonomous vehicles under various road frictions and vehicle speeds," *IEEE Trans. Intell. Veh.*, vol. 8, no. 2, pp. 1252–1265, 2023.

[38] Y. Liu, X. Pei, H. Zhou, and X. Guo, "Spatiotemporal trajectory planning for autonomous vehicle based on reachable set and iterative LQR," *IEEE Trans. Veh. Technol.*, vol. 73, no. 8, pp. 10 932–10 947, 2024.

[39] R. Chai, D. Liu, T. Liu, A. Tsourdos, Y. Xia, and S. Chai, "Deep learning-based trajectory planning and control for autonomous ground vehicle parking maneuver," *IEEE Trans. Autom. Sci. Eng.*, vol. 20, no. 3, pp. 1633–1647, 2023.

[40] H. Lin, Y. Han, W. Cai, and B. Jin, "Traffic signal optimization based on fuzzy control and differential evolution algorithm," *IEEE Trans. Intell. Transp. Syst.*, vol. 24, no. 8, pp. 8555–8566, 2023.

[41] R. Hult, M. Zanon, S. Gros, and P. Falcone, "A semidistributed interior point algorithm for optimal coordination of automated vehicles at intersections," *IEEE Trans. Control Syst. Technol.*, vol. 30, no. 5, pp. 1977–1989, 2022.

[42] J. Tang, Y. Yang, W. Hao, F. Liu, and Y. Wang, "A data-driven timetable optimization of urban bus line based on multi-objective genetic algorithm," *IEEE Trans. Intell. Transp. Syst.*, vol. 22, no. 4, pp. 2417–2429, 2021.

Zhihao Lin has received an M.S. degree from the College of Electronic Science & Engineering, Jilin University, Jilin, China. He is currently pursuing a Ph.D. degree with the James Watt School of Engineering, University of Glasgow, Glasgow. His main research interests focus on multi-sensor fusion SLAM systems and hybrid control of vehicle platoons.

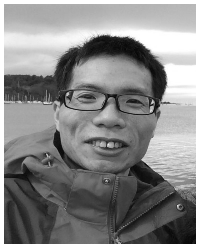

Jianglin Lan received the Ph.D. degree from the University of Hull in 2017. He has been a Lecturer and Leverhulme Early Career Fellow at the University of Glasgow since 2022. He was a Visiting Professor at the Robotics Institute, Carnegie Mellon University, in 2023. From 2017 to 2022, he held postdoc positions at Imperial College London, Loughborough University, and University of Sheffield. He is an Editor for the International Journal of Adaptive Control and Signal Processing.

Anh-Tu Nguyen (Senior Member, IEEE) received the Engineering degree and Master degree in Automatic Control from Grenoble Institute of Technology in 2009, and the Ph.D. degree in Automatic Control from Université Polytechnique Hauts-de-France in 2013. He is currently an Associate Professor with INSA Hauts-de-France, Université Polytechnique Hauts-de-France. His research interests include robust control and estimation, human-in-the-loop control, and mechatronic applications. He is an Associate Editor of IEEE/ASME Transactions on Mechatronics, IEEE Transactions on Intelligent Transportation Systems, Control Engineering Practice, and ISA Transactions.

David Flynn received the B.Eng. degree (Hons.) in Electrical and Electronic Engineering, the M.Sc. degree (Distinction) in Microsystems, and the Ph.D. degree in Microscale Magnetic Components from Heriot-Watt University in 2002, 2003, and 2007, respectively. He is a Professor of Cyber Physical Systems at University of Glasgow. He is a co-founder of the UK's EPSRC National Centre for Energy System Integration and the UK Offshore Robotics and Artificial Intelligence Hub for Offshore Energy Asset Integrity Management.